

Structure and dynamics of a wave train along the wintertime Asian jet and its impact on East Asian climate

Kaiming Hu¹ · Gang Huang^{1,2,3} · Renguang Wu¹ · Lin Wang¹

Received: 18 November 2016 / Accepted: 31 March 2017 / Published online: 18 April 2017
© Springer-Verlag Berlin Heidelberg 2017

Abstract Based on observational and reanalysis datasets, this study investigates the structure and dynamics of a wave-like atmospheric teleconnection pattern along the wintertime Asian jet and its influence on East Asian climate. Along the jet, the leading empirical orthogonal function (EOF) mode of monthly meridional winds at 250-hPa in winter (December, January, and February) is organized as a wave train with maximum anomalies at upper troposphere. The wave train propagates northeastward from the North Atlantic to Europe, turns southeastward to the Middle East with amplifying amplitude, propagates along the jet to South China, and reaches Japan, which is partly induced by sea surface temperature (SST) anomalies in the equatorial eastern Pacific and the North Atlantic Oscillation. Over the sector from Europe to the Middle East, the anomalous vortices in the wave train tilt northwestward

with height and tilt northeast/southwest in horizontal at 250 hPa, favoring for extracting available potential energy and kinetic energy from mean flows effectively. In addition, there exists a positive feedback between transient eddies and the wave train-related anomalous circulation over the North Atlantic and Europe. These processes help to maintain and amplify the wave train. Moreover, the wave train can exert significant influences on the wintertime climate in East Asia. When it is in the phase with a cyclone (anticyclone) over South China (Japan), rainfall tends to be above normal in South and East China and surface air temperature tends to be above normal around Japan and the Korea peninsula.

Keywords Wave train · Wintertime Asian Jet · East Asian climate

This paper is a contribution to the special issue on East Asian Climate under Global Warming: Understanding and Projection, consisting of papers from the East Asian Climate (EAC) community and the 13th EAC International Workshop in Beijing, China on 24–25 March 2016, and coordinated by Jianping Li, Huang-Hsiung Hsu, Wei-Chyung Wang, Kyung-Ja Ha, Tim Li, and Akio Kitoh.

✉ Gang Huang
hg@mail.iap.ac.cn

¹ Center for Monsoon System Research and State Key Laboratory of Numerical Modeling for Atmospheric Sciences and Geophysical Fluid Dynamics, Institute of Atmospheric Physics, Chinese Academy of Sciences, P.O. Box 9804, Beijing 100029, China

² Joint Center for Global Change Studies (JCGCS), Beijing 100875, China

³ University of Chinese Academy of Sciences, Beijing 100049, China

1 Introduction

The stationary Rossby wave can propagate along strong westerly jets (Hoskins and Ambrizzi 1993). This is because that the jet regions exhibit strong maxima in the wavenumber of stationary Rossby wave, with minima to the north and south of the jets. Since Rossby wave rays are always refracted toward latitudes with larger stationary wavenumber, the stationary Rossby wave tends to be refracted toward the core of the jet, indicating that the jet acts as an efficient waveguide.

There are strong westerly jets over Asia in both boreal winter and summer. In summer, the Asian jet is located around 40°N. Lu et al. (2002) reported that stationary wave activities in summer Asian jet have a favored longitudinal phase. This wave train, which was subsequent named as a silk road teleconnection by Enomoto et al. (2003),

could lead to anomalous rainfall and temperature over North China (Huang et al. 2011; Chen and Huang 2012) and Japan (Sato and Takahashi 2006). The geographical fixing of silk road teleconnection is possibly because it is triggered by geographically-fixed convective activities to the north of the Arabian Sea (Ding and Wang 2005), and because the pattern of teleconnection has the most efficiency to extract kinetic and available potential energy from mean flow (Kosaka et al. 2009).

In boreal winter, the Asian jet shifts southward to the latitudes around 25°N, extending from the Middle Asia to the North Pacific. Branstator (2002) proved that the winter Asian jet could provide a waveguide for stationary Rossby waves. Using model simulations, he suggested that the stationary Rossby waves in the jet have no favored longitudinal phase as the first two leading empirical orthogonal function (EOF) modes cannot be distinguished with each other. But in his observational analyses, stationary Rossby waves in the jet appear to have a favored phase, which he thought is possibly caused by sample deficient in the observations. In the later studies, researchers mainly focus on the role of the jet to extend upstream perturbation to downstream regions via wave propagation (Watanabe 2004; Song et al. 2013; Li and Zhou 2016; Li and Sun 2015), while whether the wave activities along the jet have a preferable longitudinal phase is still unresolved.

Following the observational analyses in Branstator (2002), we have detected a wave train in the jet with preferable longitudinal phase. To establish confidence in the existence of the wave train, we have investigated the mechanism for how the wave train develops. To do that, we first examined whether the wave train is an optimal atmospheric internal model that easily gains energy from mean flows and transient eddies. Then, we examined whether the wave train is anchored by geographically-fixed external forcing. We mainly focused on two kinds of external forcing in this study: the North Atlantic Oscillation (NAO) and tropical sea surface temperature, because evidences (Branstator 2002; Watanabe 2004; Song et al. 2013) show that wave activities in the jet are partly linked to the North Atlantic Oscillation (NAO), which in turn is likely affected by tropical perturbations (Lin et al. 2005; Li and Lau 2012; Yu and Lin 2016). Moreover, we have investigated the impact of the wave train on East Asian climate.

The paper is organized as follows. Section 2 provides a brief description of datasets and methods. Sections 3 and 4 show spatial pattern and vorticity budget of the leading wave train in the jet. In Sect. 5, we analyze the conversions of kinetic energy and available potential energy from mean flow to the leading wave train. In Sect. 6, we investigate the feedback between transient eddies and the leading wave train. In Sect. 7, we examine the possible external forcing for the leading wave train. Section 8 shows the impact of

the wave train on wintertime temperature and precipitation in East Asia. Finally, we give a summary in Sect. 9.

2 Data and methods

The monthly and daily mean winds, geopotential height, air temperature are derived from the National Centers for Environmental Prediction-Department of Energy (NCEP-DOE) atmospheric reanalysis dataset with a resolution of $2.5^\circ \times 2.5^\circ$, which is available from 1979 to present (Kanamitsu et al. 2002). The global precipitation dataset used in this study is the Global Precipitation Climatology Project (GPCP) monthly precipitation dataset available from 1979, which combines observations and satellite precipitation data into $2.5^\circ \times 2.5^\circ$ global grids (Adler et al. 2003). The China monthly mean precipitation dataset used in this study includes 160 stations in China for the period 1979–2013, which was provided by the National Climate Center, China Meteorological Administration.

The stationary Rossby waves trapped by the wintertime Asian jet waveguide can persist longer than 10 days and can be easily identified in monthly mean data (Watanabe 2004). Thus, we analyze the structure and dynamics of stationary waves in winter months (December, January, and February, DJF) during 1979/80–2013/14, constituting 105 months. Before analyses, we remove annual cycle from raw data to obtain monthly anomalies. Given autocorrelations of monthly time series could reduce effective sample sizes when testing statistical significance, following Metz (1991), we calculate effective sample sizes N_{eff} for correlations and regressions of time series X and Y as

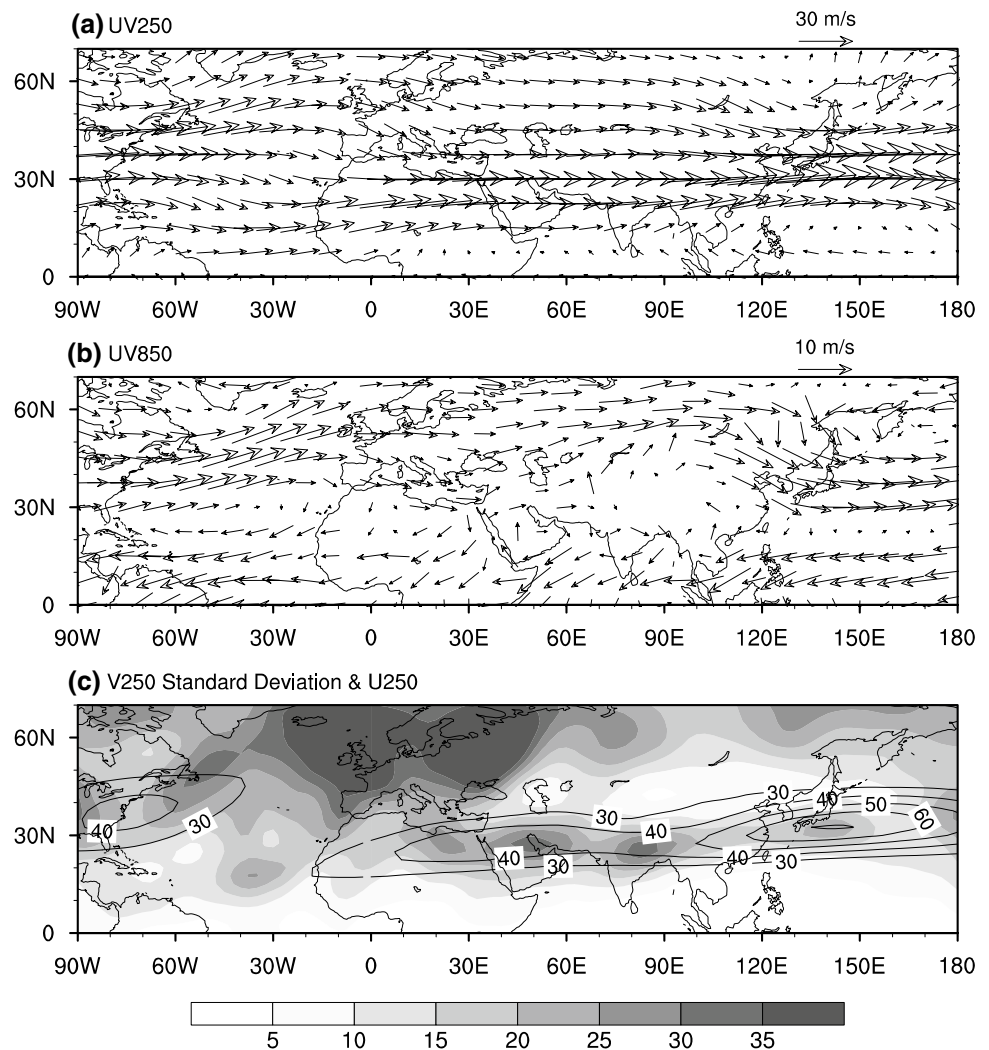
$$N_{eff} = N / \max \left[1, 1 + 2 \sum_{\tau=1}^{\tau_{max}} \left(1 - \frac{\tau}{N} \right) r_X(\tau) r_Y(\tau) \right], \quad (1)$$

where N denotes the sample sizes, and $r_X(\tau)$ and $r_Y(\tau)$ are the autocorrelations of time series X and Y with a lag of τ months. The maximum lag τ_{max} is set as the maximum number that does not exceed $N/2$. In this study, all the statistical significances are evaluated with a two-sided Student's t test, taking into consideration of the effective sample sizes.

3 Structure of the leading wave train

Climatological mean winds at 250- and 850-hPa are shown in Fig. 1a, b. At the lower troposphere, there are strong northwesterlies from the Siberia to Japan and strong northeasterlies from the subtropical Northwest Pacific to the Maritime Continent. At upper troposphere, there are strong westerlies from North Africa to the subtropical Northwest

Fig. 1 The climatology of DJF winds at 250-hPa (a) and 850-hPa (b), and the standard deviation (grays) of DJF monthly v at 250-hPa overlaid by DJF mean u (contours; m/s) at 250-hPa (c)

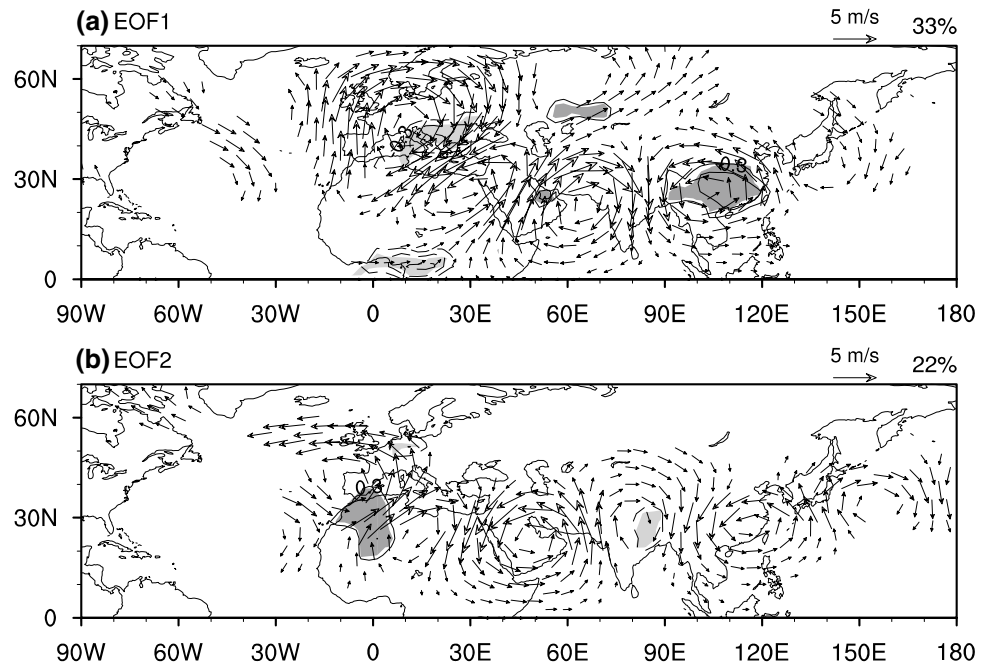


Pacific, known as wintertime Asian jet, with the maximum wind speed exceeding 45 m s^{-1} . The jet can provide a favorable waveguide for stationary Rossby wave propagation (Hoskins and Ambrizzi 1993; Branstator 2002). Figure 1c shows the standard deviations of monthly (DJF) meridional winds (v) at 250-hPa. The standard deviations are larger in the jet than its adjacent regions, indicating that wave activities are strong along the jet. Moreover, the standard deviations of v along the jet are not uniform but have multiple centers of great value over Egypt, the Persian Gulf, North Indian and the sea to the south of Japan. Outside the jet, the variability of monthly mean v is large at high latitudes especially in the sector from the North Atlantic to Europe, suggesting strong wave activities there.

In order to investigate the spatial pattern of wave activities along the jet, we perform an empirical orthogonal function (EOF) analysis based on monthly (DJF) v at 250-hPa in the domain of $0\text{--}45^\circ\text{N}$, $0\text{--}120^\circ\text{E}$ from 1979 to 2013, following Branstator (2002). The first and second EOF modes account for 33 and 22% of the total variance, respectively,

which can be distinguished with each other based on criterion of North et al. (1982), consistent with Branstator (2002). The results, together with that the standard deviations of v along the jet are not uniform but have multiple centers, indicate that the two EOF modes are two discrete modes but not the components of a continuous Rossby wave family. Figure 2a, b show the regressions of winds at 250-hPa onto the first and second principal component (PC1 and PC2), respectively. For simplicity, we use the regressions of winds onto PC1 and PC2 to represent the first and second leading EOF (EOF1 and EOF2) modes here (Fig. 2). The EOF1 mode features a wave-like structure with an anticyclone over the subtropical Northwest Atlantic, a cyclone over the North Atlantic, an anticyclone over Europe, a cyclone over Egypt, an anticyclone over the Arabian Gulf, a cyclone over South China, and an anticyclone over Japan. It is noted that the EOF1 mode is not a local atmospheric mode only confined in the jet but has a substantial part in the sector from the North Atlantic to Europe. Compared with EOF1 mode, the zonal phase of

Fig. 2 The regression of monthly 250-hPa winds (vectors; above 99% confidence level) onto the PC1 (a) and PC2 (b) of the EOF modes of 250-hPa monthly v (December, January, and February) in the domain (0–45°N, 0–120°E) from 1979 to 2013. The contours in a (b) represent the correlations of monthly precipitation with PC1 (PC2), with shades above 99% confidence level. The first and second leading EOF modes explain 33 and 22% of total variance, respectively



EOF2 mode is shifted westward about a quarter wavelength from EOF1 mode. We note that the great value centers of monthly v variability over the North Africa, the Middle East and the South Asia are corresponding to EOF1 mode, indicating that the wind anomalies in the jet are most likely to be developed into EOF1 mode.

The contours in Fig. 2a, b represent the correlations of precipitation with PC1 and PC2, respectively. In the Northern Hemisphere, the most significant correlation of precipitation with PC1 is located in South and East China, with correlation coefficients exceeding the 99% confidence level. When EOF1 mode is in its positive (negative) phase, the rainfall in South and East China is significantly above (below) normal (Fig. 2a). Compared with PC1, the correlations of precipitation with PC2 are weak especially over East Asia (Fig. 2b). Since the EOF1 mode is the leading mode of wave activities and since the EOF1 mode exerts a strong influence on East Asian wintertime precipitation, we will only investigate EOF1 mode and its impact in the following sections.

Figure 3 shows the wave-activity fluxes and height anomalies associated with the EOF1 mode, where the definition of the wave-activity fluxes follows Takaya and Nakamura (2001) as:

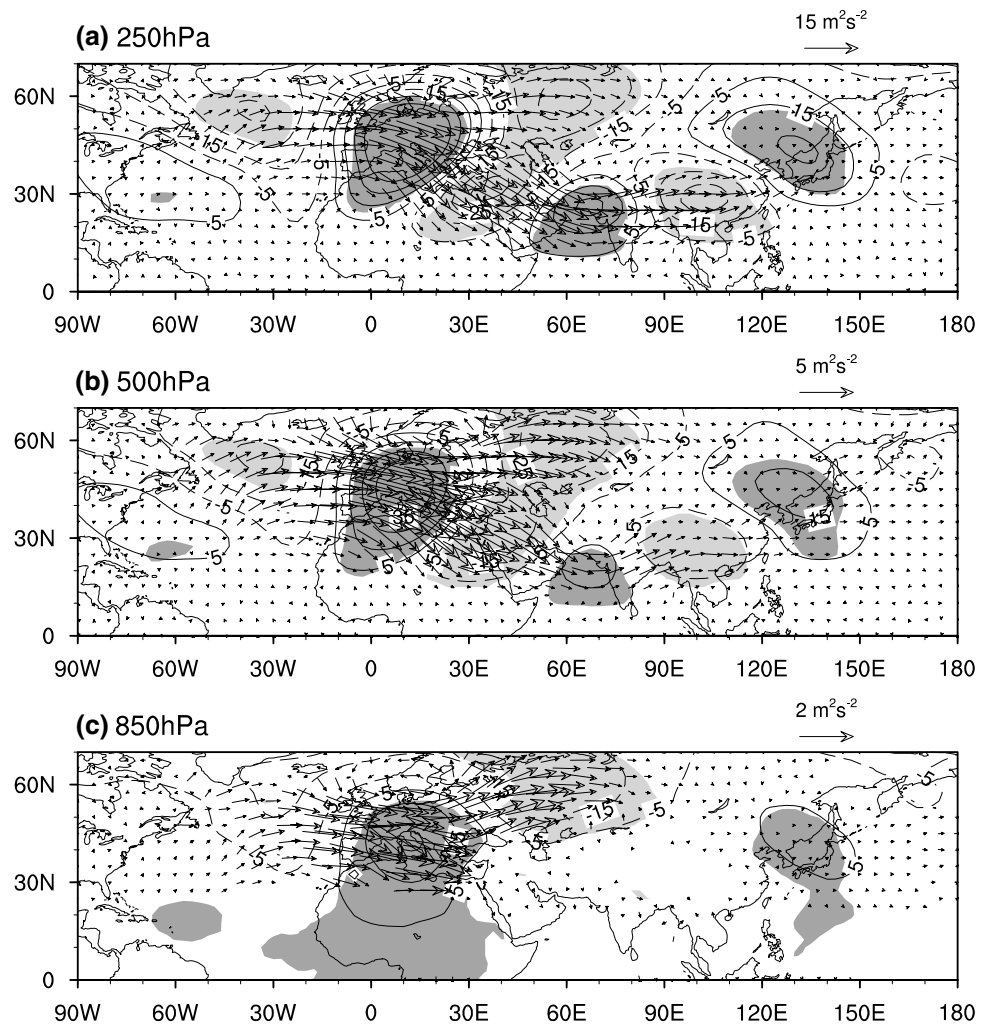
$$W = \frac{1}{2|U|} \left(\begin{array}{l} \bar{u}(\psi_x'^2 - \psi' \psi_{xx}') + \bar{v}(\psi_x' \psi_y' - \psi' \psi_{xy}') \\ \bar{u}(\psi_x' \psi_y' - \psi' \psi_{xy}') + \bar{v}(\psi_y'^2 - \psi' \psi_{yy}') \\ \frac{f^2}{R\sigma/p} \left\{ \bar{u}(\psi_x' \psi_p' - \psi' \psi_{xp}') + \bar{v}(\psi_y' \psi_p' - \psi' \psi_{yp}') \right\} \end{array} \right) \quad (2)$$

Here, ψ denotes the stream function, f the Coriolis parameter, R the gas constant, $U = (u, v)$ the horizontal

wind velocity, and $\sigma = (R\bar{T}/C_p p) - d\bar{T}/dp$, with temperature T , and the specific heat at constant pressure C_p . Overbars and primes denote the DJF mean and the monthly disturbances regressed on normalized PC1, respectively. The fluxes are parallel to the local group velocity of stationary Rossby wave. At 250-hPa, the wave activity fluxes start from the North Atlantic intensifying over Europe, pass through the Mediterranean, turn southeastward to the Arabian Sea, cross South Asia and turn northeastward to Japan, in consistent with wave-like geopotential height anomalies. At 500-hPa, the patterns of wave activity fluxes and the geopotential height anomalies are similar with those at 250-hPa. At 850-hPa, the wave activity fluxes are weak in the jet regions, so are the geopotential height anomalies. Outside the jet, there are strong wave activity fluxes over the Siberia, which seems to be corresponding to strong westerlies there (Fig. 1b). Thus, there likely exist two paths of wave propagation from Europe to East Asia. One path is the Asian jet at upper troposphere, and the other is at high-latitudes around 60°N. The wave activities along the jet are mainly confined at the mid and upper troposphere, while the wave activities at high-latitudes are strong in lower troposphere corresponding to the strong westerlies there.

Figure 4 shows a longitude-height section of vorticity, temperature and vertical velocity anomalies associated with the wave train at the latitude of 25°N. The selection of 25°N is because it is the central latitude of climatological Asian jet. It is important to note that the wave pattern in the North Atlantic and Europe is away from 25°N, so Fig. 4 only displays the vertical structure of waves that locate within the jet. To the east of 10°E, there are three obvious anomalous

Fig. 3 The regressions of geopotential height (contours; unit: m) at 250-hPa (a), 500-hPa (b) and 850-hPa (c) on the PC1. Vectors are the wave fluxes computed by the Eq. (2). The dark (light) grays represent positive (negative) regression above 99% confidence level



vorticity cells (Fig. 4a), corresponding to the anticyclonic anomalies over the Arabian Gulf and the cyclonic anomalies over Egypt and South China. The vorticity anomalies increase with height and peak at around 250-hPa. In detail, the vorticity anomalies tilt westward with height to the west of 60°E and tilt eastward slightly to the east of 60°E, corresponding to the upward (downward) wave fluxes to the west (east) of 60°E. According to the thermal wind relation, the vertical change of vorticity must be associated with air temperature anomalies, with warmer (cooler) air under upper positive (negative) vorticity anomalies (Fig. 4b).

4 Vorticity budget of the leading wave train

In this section, we conduct an analysis of the vorticity budget based on the linearized vorticity equation (Kosaka and Nakamura 2006):

$$S - \underbrace{\bar{u}_\psi \frac{\partial \zeta'}{\partial x}}_{ZA} - \underbrace{\bar{v}_\psi \frac{\partial \zeta'}{\partial y}}_{MA} - \underbrace{u'_\psi \frac{\partial \bar{\zeta}}{\partial x} + v'_\psi \frac{\partial (f + \bar{\zeta})}{\partial y}}_{\beta} - (\text{residuals}) = 0, \quad (3)$$

where S represents the linearized barotropic Rossby wave source (Sardeshmukh and Hoskins 1988):

$$S = -\nabla_H \cdot \left\{ \mathbf{u}'_\chi (f + \bar{\zeta}) \right\} - \nabla_H \cdot (\bar{\mathbf{u}}_\chi \zeta'). \quad (4)$$

In Eqs. 3 and 4, $\mathbf{u}_\psi = (u_\psi, v_\psi)$ and $\mathbf{u}_\chi = (u_\chi, v_\chi)$ are the rotational and divergent wind components, respectively, and ζ denotes relative vorticity. The terms ZA and MA represent the advections of anomalous vorticity by climatological zonal and meridional winds, respectively, and the β term represents the horizontal advection of the mean absolute vorticity by anomalous winds. Vertical advection, tilting and nonlinear effects are included in the residuals. A positive value of a specific term corresponds to an increasing tendency of cyclonic vorticity.

Fig. 4 The longitude-height section of vorticity anomalies (a) with interval $2(\pm 1, \pm 3, \pm 5, \dots) \times 10^{-6} \text{ s}^{-1}$, air temperature anomalies (b) with interval $0.2(\pm 0.1, \pm 0.3, \pm 0.5, \dots) \text{ K}$, and vertical motion anomalies (c) with interval $0.5(\pm 0.5, \pm 1, \pm 1.5, \dots) \times 10^{-2} \text{ Pa s}^{-1}$ regressed on the normalized PC1. The vectors denote wave fluxes. The dark (light) shades represent positive (negative) correlations above 99% confidence level

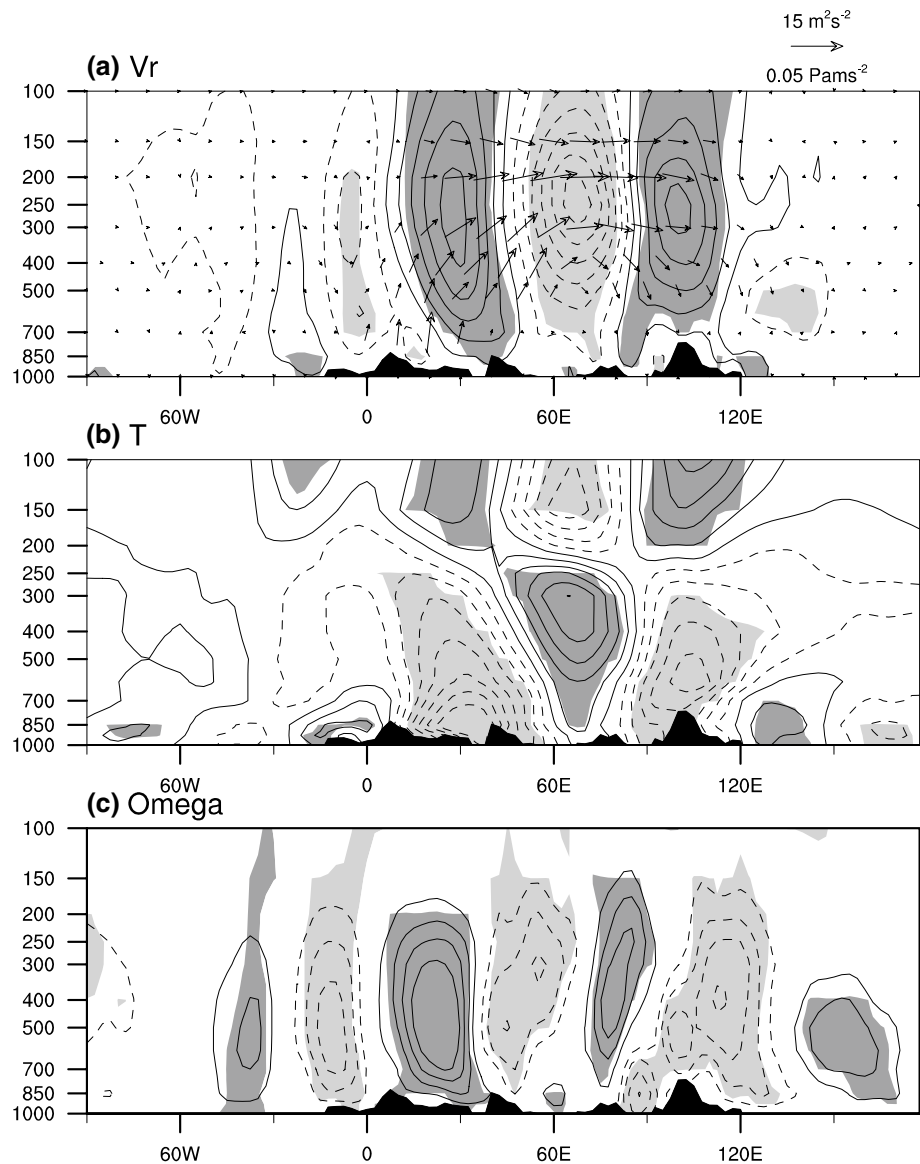


Figure 5a–d show the contribution of each term at 250-hPa based on the regression of wind anomalies on normalized PC1. There are alternate positive and negative wave sources along the jet (Fig. 5a), with cyclonic vorticity sources over the east of Mediterranean regions, South Asia and the sea to the east of Japan and anticyclonic vorticity sources over the Middle East and East Asia. We note that the strongest wave source is over the Mediterranean, which may in turn partly link with the North Atlantic Oscillation (Watanabe 2004). The terms of ZA (Fig. 5b) and β (Fig. 5d) are much stronger than the others in the jet, and their signs are opposite to each other. This suggests that the advection of perturbation vorticity by mean flow tends to be compensated by β effect, indicating the wave along the jet is indeed a stationary Rossby wave. We also examine the value of

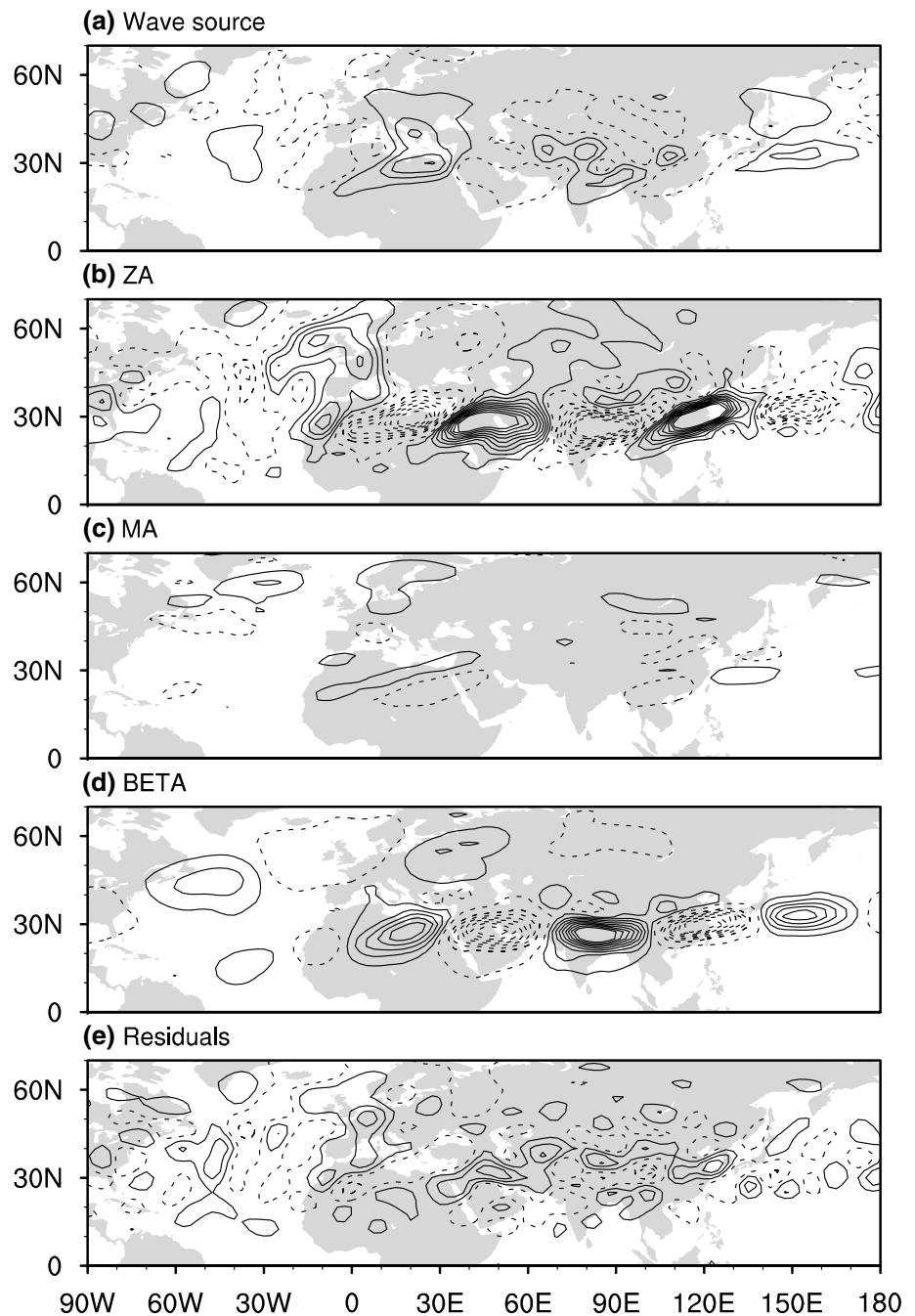
$-u'_{\psi} \frac{\partial \bar{\zeta}}{\partial x}$ and $-v'_{\psi} \frac{\partial (f + \bar{\zeta})}{\partial y}$ in the β term, and find that the β term is mainly contributed by $-v'_{\psi} \frac{\partial (f + \bar{\zeta})}{\partial y}$ (not shown). The

MA term (Fig. 5c) is too weak to contribute much to the teleconnection. The values of residuals are small and scattered (Fig. 5e), indicating it does not play an important role in the vorticity budget.

5 Energy conversions between the perturbations of leading wave train and mean flows

In this section, we estimate the conversion of local kinetic energy (CK) and the conversion of available potential energy (CP) associated with EOF1 mode. Our evaluation is based on

Fig. 5 The Rossby wave source (a), the zonal advection term (b), the meridional advection term (c), the β term (d), and the residuals (e) in the linearized vorticity Eq. (3), based on the regressions of 250-hPa winds on the normalized PC1. Solid (dash) contours denote positive (negative) values, with interval 4 ($\pm 2, \pm 6, \pm 10, \dots$) $\times 10^{-11} \text{ s}^{-2}$



the following equations, the same as those used by Kosaka and Nakamura (2006):

$$CK = \frac{v'^2 - u'^2}{2} \left(\frac{\partial \bar{u}}{\partial x} - \frac{\partial \bar{v}}{\partial y} \right) - u'v' \left(\frac{\partial \bar{u}}{\partial y} + \frac{\partial \bar{v}}{\partial x} \right), \quad (5)$$

$$CP = -\frac{f}{\sigma} v' T' \frac{\partial \bar{u}}{\partial P} \frac{f}{\sigma} u' T' \frac{\partial \bar{v}}{\partial P}. \quad (6)$$

Here, positive CK and CP mean the conversion of kinetic energy and available potential energy from mean flow to the wave train, respectively.

As the vorticity anomalies of the wave train extend to 100-hPa (Fig. 4), we calculate the vertical integral of CK and CP from the surface to 100-hPa to denote conversion of local kinetic energy and available potential energy between the wave train and mean flow (Fig. 6). The most prominent CK and CP are located from 10°W to 150°E . To the east of 50°E , both CK and CP are alternatively positive and negative along the jet, and the total CK and CP in this region is close to zero. To the west of 50°E , where dominant term in Eq. (5) is $u'v' \frac{\partial \bar{u}}{\partial y}$, positive CK is

Fig. 6 **a** Vertically integrated (from surface to 100-hPa) conversion of kinetic energy with interval $1 (\pm 0.5, \pm 1.5, \pm 2.5, \dots) \times 10^{-1} \text{ Wm}^{-2}$. **b** Vertically integrated (from surface to 100-hPa) conversion of available potential energy with interval $0.5 (\pm 0.25, \pm 0.75, \pm 1.25, \dots) \times 10^{-1} \text{ Wm}^{-2}$. The vectors denote wave fluxes at 250-hPa, and the grays represent DJF mean zonal wind speeds above 35 m/s. The rectangle to the west (east) of 50°E represents the upstream (downstream) of the wave train

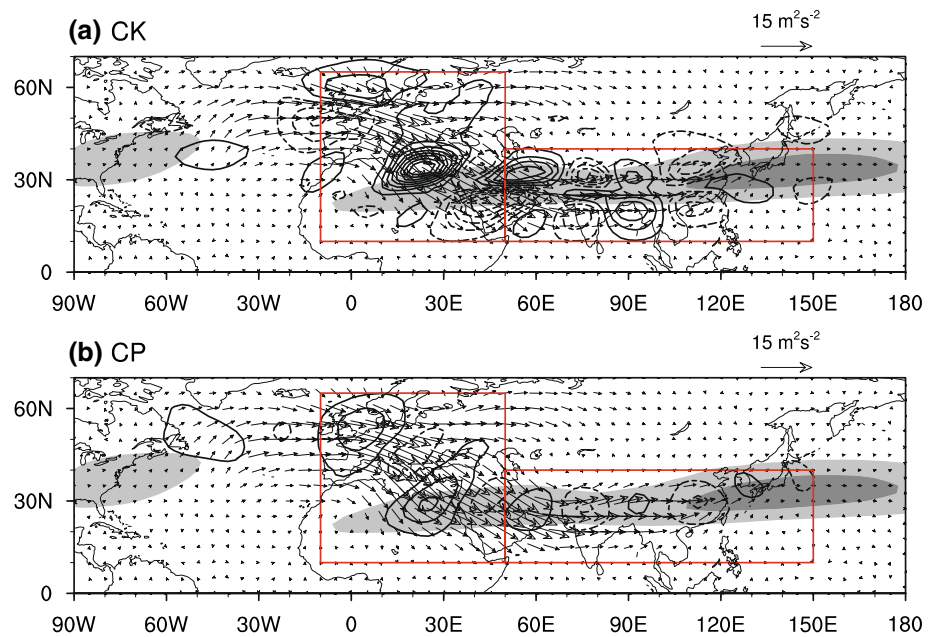


Table 1 Area mean of vertically integrated (from surface to 100 hPa) *CK* and *CP* (Wm^{-2}) in the North Hemisphere after the wave pattern is shifted longitudinally relative to the original location

	20° west-ward	10° west-ward	Original	10° east-ward	20° eastward
<i>CK</i>	0.0018	0.0017	0.0022	0.0013	-0.0016
<i>CP</i>	0.0017	0.0018	0.0020	0.0019	0.0016

mainly distributed to the north side of mean jet while negative *CK* is mainly distributed to the south side of mean jet, and positive *CP* is mainly located in Northwest Europe and the regions around the east part of Mediterranean while negative *CP* is mainly located to the north of Mediterranean. We note that positive *CP* and *CK* are obviously larger than negative *CP* and *CK* in the sector from Europe to the Middle East, indicating that the wave train can get kinetic energy and available potential energy from the mean flow in this region.

Thus, we divide the regions of the wave train into two parts: the upstream region (10°N – 65°N , 10°W – 50°E) and the downstream region (10°N – 40°N , 50°E – 150°E). The area mean of vertically integrated *CK* and *CP* are 2.35×10^{-2} and $1.62 \times 10^{-2} \text{ Wm}^{-2}$ in the upstream region, and -2.7×10^{-3} and $-3.56 \times 10^{-3} \text{ Wm}^{-2}$ in the downstream region, respectively. Here, we divided the upstream and the downstream by 50°E , where is the turning point from southeastward wave propagation to eastward propagation. We also test different dividing longitudes, and find that the area-mean values of vertically integrated *CK* and *CP* in the upstream and downstream are not very sensitive to the selection of dividing longitudes. Both of

CK and *CP* are acting to strengthen the wave train in the upstream region but to damp the wave train in the downstream region. The area-mean values of the vertically integrated *CK* and *CP* over the entire North Hemisphere are 2.15×10^{-3} , and $1.98 \times 10^{-3} \text{ Wm}^{-2}$, respectively. Thus, the net effects of both of *CK* and *CP* are favorable for the maintenance of the wave train. In order to investigate a possible role of energy conversions in the geographic fixing of the longitudinal phase of the wave train, we calculated area mean of vertically integrated *CK* and *CP* in the North Hemisphere (Table 1) after the wave pattern are shifted longitudinally relative to the original location following Kosaka et al. (2009). Both the values of area-mean *CK* and *CP* are largest when the pattern is in its original location, suggesting energy conversions help to anchor the wave train in its favored phase.

To measure the net contribution of *CK* and *CP* to the maintenance of the teleconnection, we evaluate the time scales: $\tau_{CK} = \frac{[KE]}{CK}$ and $\tau_{CP} = \frac{[APE]}{CP}$, where the bracket $\langle \rangle$ represents area mean, $[APE] = [RT'^2/2\sigma p]$ is vertically integrated available potential energy (from surface to 100-hPa) associated with the teleconnection, and $[KE] = [(u'^2 + v'^2)/2]$ is vertically integrated kinetic energy. The values of τ_{CK} and τ_{CP} denote how long it takes that the available potential energy and kinetic energy associated with the teleconnection could be fully replenished through *CK* and *CP*, respectively. The τ_{CK} is 8.58 days in the upstream region, -36.5 days in the downstream region, and 25.3 days in the North Hemisphere. The τ_{CP} is 1.1 days in the upstream region, -1.5 days in the downstream region and 2.4 days in the North Hemisphere. Both τ_{CK} and τ_{CP} are shorter than a month in the North Hemisphere, indicating

that energy conversion, especially in the upstream region, is vital to the maintenance of the wave train.

Why can the wave train extract kinetic energy and available potential energy effectively from mean flows in the upstream region? First, we examine the conversion of local kinetic energy in this region. To the west of 50°E, the anomalous anticyclone and cyclone in the wave train tilt northeast/southwest in horizontal (Fig. 2a), leading to northward fluxes of zonal momentum ($u'v' > 0$), resulting in negative values of $u'v' \frac{\partial \bar{u}}{\partial y}$ in the north flank of mean jet and positive values of $u'v' \frac{\partial \bar{u}}{\partial y}$ in the south flank of mean jet. According to the Eq. (5),

the perturbations could gain kinetic energy from mean flow in the north flank of mean jet and release energy in the south flank. As the perturbations are mainly distributed in the north flank of jet to the west of 50°E, the total value of CK there is positive. Thus, the positive CK is caused by the special spatial structure of perturbations, which is in turn related to southward wave propagation. Second, we check CP in this region. Figure 7 shows the vertical section of vorticity and temperature anomalies from the point (65°N, 10°W) to the point (10°N, 50°E) along the direction of wave train propagation. The vorticity anomalies are not totally barotropic but slightly tilt northwestward with the increase of height, accompanied with positive (negative) air temperature anomalies to the northwest of negative (positive) anomalous vorticity

center. Such vertical structure of vorticity and temperature anomalies is favorable for positive CP in the regions from the Europe to the Middle East, where exists prominent zonal temperature gradient, as $v'T'$ tends to weaken the mean temperature gradient. The results suggest that energy conversion in the region from Europe to the Middle East is vital for the development and the geographic fixing of the wave train.

6 Interaction between transient eddies and the leading wave train

To investigate the interaction between synoptic-scale transient eddies and the wave train, several diagnostic tools are utilized. The first is the local Eliassen-Palm vectors (E), formulated by Hoskins et al. (1983), with horizontal components given by $(\overline{v'^2} - \overline{u'^2}, -\overline{v'u'})$, where u' and v' are the synoptic-scale daily 250-hPa winds subject to 2.5–6 days band filtering, the overbar represents time average of a month. The direction of E is linked to the direction of group propagation vector of the synoptic-scale eddies relative to the mean flow. Here, divergence (convergence) of E indicates a tendency for the high-frequency perturbation to accelerate (decelerate) the monthly mean flow. The second is the eddy-induced geopotential height tendency defined in Lau and Nath (2014) and shown in Eq. 7:

Fig. 7 **a** The vertical section of vorticity anomalies regressed onto PC1 (dash lines < 0 ; thick solid line $= 0$; thin solid line > 0) with interval $2 (0, \pm 2, \pm 4, \pm 6, \dots) \times 10^{-6} \text{ s}^{-1}$ from the point (65°N, 10°W) to the point (10°N, 50°E). **b** Same as **a**, but for air temperature anomalies at interval of 0.2 K. The light (dark) grays denote negative (positive) regressions above 99% confidence level

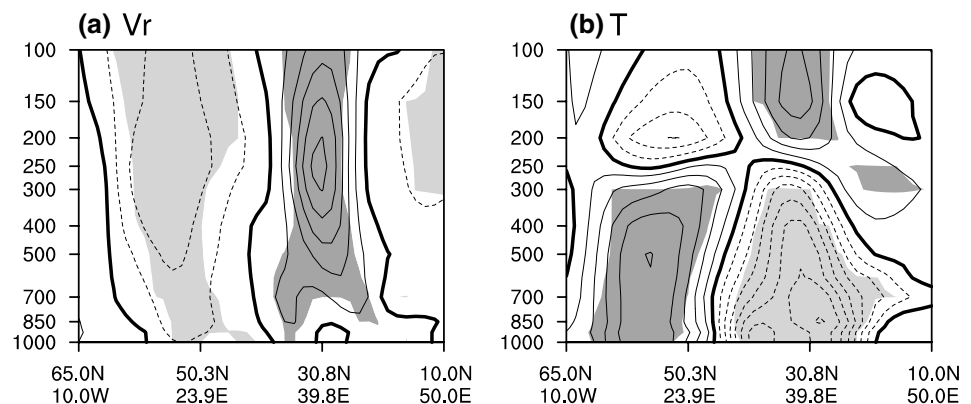
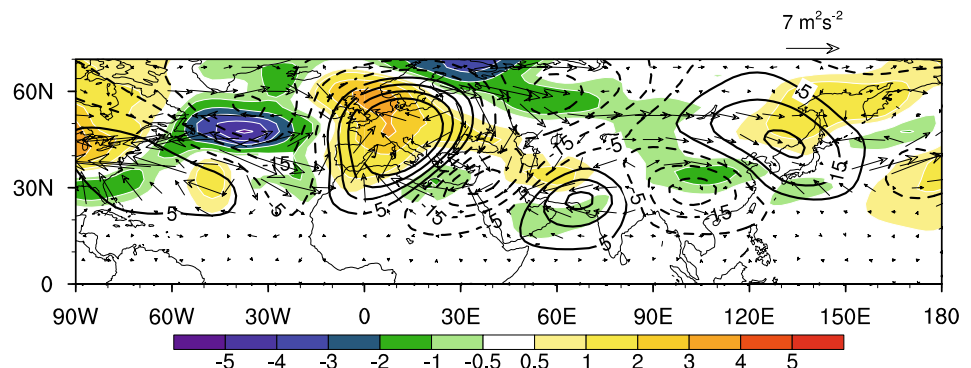


Fig. 8 The regressions of geopotential height at 250 hPa (contours; m), E vectors ($\overline{v'^2} - \overline{u'^2}$, $-\overline{v'u'}$), and transient eddy-induced height tendencies (colors; m/day) on the normalized PC1



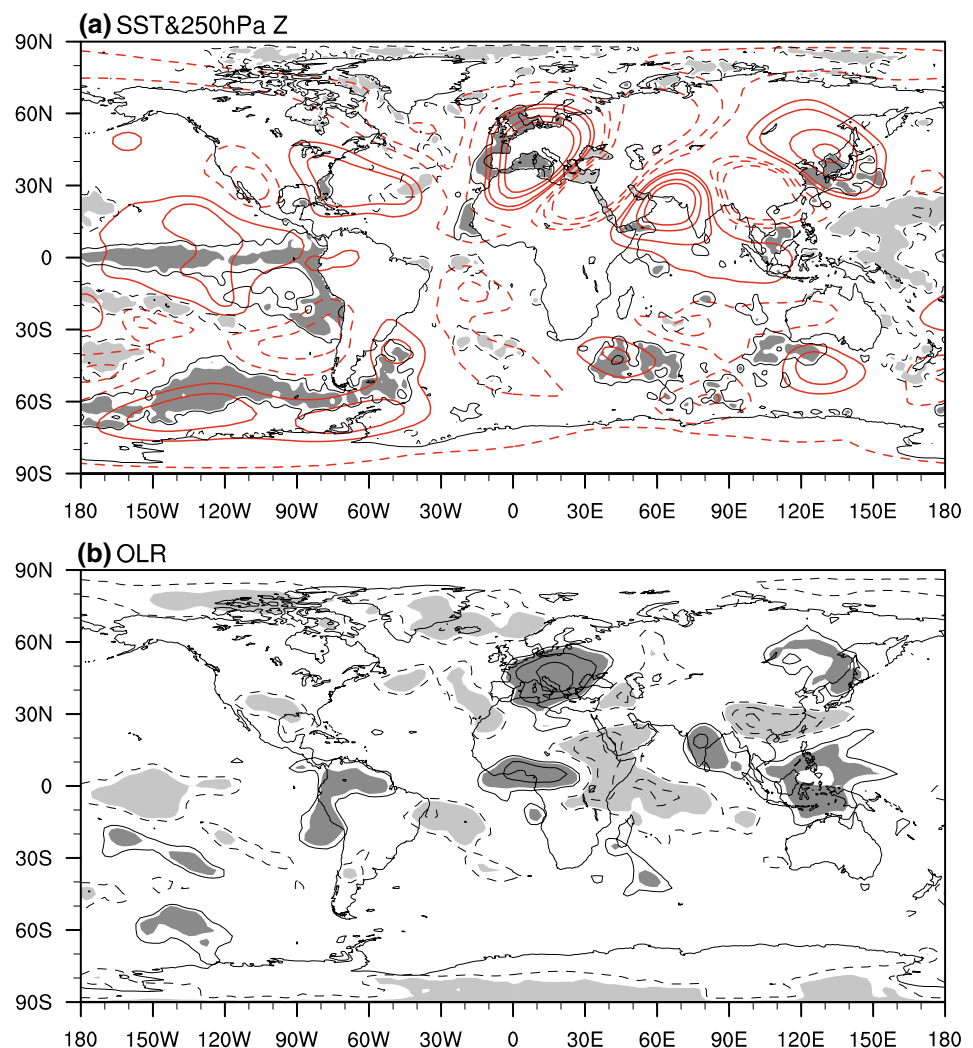
$$\left(\frac{\partial Z}{\partial t}\right)_{\text{eddy}} = \frac{f}{g} \nabla^{-2} [-\nabla \cdot (\overline{V' \zeta'})] \quad (7)$$

where Z is the monthly mean geopotential height, g is the gravitational acceleration, and V' and ζ' are the synoptic-scale daily winds and relative vorticity at 250-hPa subject to 2.5–6 days band filtering. The meaning of the overbar is the same as in the definition of E . This diagnostic tool was also used in our previous studies (Liu et al. 2014; Song et al. 2016).

Figure 8 shows the regression of geopotential height, E vectors, and eddy-induced geopotential height tendency on normalized PC1. The geopotential height anomalies show a clear wave-like structure in accordance with EOF1 mode. In the sector of the North Atlantic and Europe, the direction E vectors is clockwise around the positive height centers, and anticlockwise around the negative centers, suggesting that the slowly varying circulation of the wave train can change the trajectory of the storm track. Over Europe, the anomalous anticyclone lets the axes of storm track shift

northward, leading to divergence of E vectors to the north of the anticyclone but convergence of E vectors in the central and the southern anticyclone (shown in Fig. 8). The divergence (convergence) of E vectors accelerates (decelerates) the westerlies in the north (south) part of the anticyclone, which can enhance the anomalous anticyclone. Hence the regions of positive height anomalies in Europe are mainly occupied by positive eddy-induced height tendencies. Ruled by the same process, the regions of negative height anomalies in the North Atlantic are mainly occupied by negative eddy-induced height tendencies. Outside the sectors of the North Atlantic and Europe, the interaction between the transient eddies and the wave train is not obvious, possibly because transient eddies are weak in these regions. These results suggest that there exists a positive feedback between transient eddies and the wave train in the North Atlantic and Europe. The stationary circulation anomalies associated with the wave train modulate the trajectory of transient eddies, which in turn reinforce the wave

Fig. 9 The correlations of DJF monthly SST (a; black contours), geopotential height (a; red contours) at 250 hPa and OLR (b; black contours) with the PC1. Solid (dash) contours denote positive (negative) values at interval 0.1 (± 0.1 , ± 0.2 , ± 0.3 , ...). The dark (light) gray shades denote positive (negative) correlations above 90% confidence level



train through eddy vorticity transports. The positive feedback may help to maintain the wave train.

7 External forcing for the wave train

Figure 9 shows the correlations of monthly SST, geopotential height, and outgoing long wave radiation (OLR) in DJF with the PC1. The most prominent SST correlations in the tropics feature an El Niño-like pattern, with correlations partly above 90% confidence level. Corresponding to positive SST correlations in the eastern equatorial Pacific, OLR correlations are negative, suggesting SST anomalies play a positive role. As a response to warm SST anomalies and positive rainfall anomalies in the equatorial eastern Pacific, the geopotential height anomalies display as a Matsuno (1966)–Gill (1980) pattern over the eastern Pacific and a wave-like pattern from the Northeast Pacific across the North Atlantic through Europe to East Asia. This result suggests that the SST anomalies in the equatorial eastern Pacific likely trigger the wave train.

Beside affected by tropical SST anomalies, the wave train is also affected by the NAO. Figure 10a, b show the relationship of the PC1 with Nino3.4 SST index and NAO index. Here, the NAO index is the PC1 of DJF monthly 850 hPa streamfunction departures from annual cycle in the North Atlantic sector (0–90°N, 90°W–30°E), same as the computing in Branstator (2002). The correlation between PC1 and Nino3.4 SST index is 0.22 for 63 effective samples, which is above 90% confidence level, and the correlation between PC1 and NAO index is 0.19 for 100 effective samples, which is also above 90% confidence level. The NAO and SST anomalies in the equatorial eastern Pacific may have a combined effect on the wave train. To quantify this combined effect, we construct a multi-variant regression: $0.26 \times \text{Nino3.4} + 0.22 \times \text{NAO}$, where Nino3.4 is the monthly (DJF) Nino3.4 SST index and NAO is the monthly (DJF) NAO index. The coefficients 0.26 and 0.22 are the multiple linear regression coefficients of the PC1 regressed onto the Nino3.4 and the NAO indices, respectively. The

multi-variant regression (Fig. 10c) is more significantly correlated with the PC1 than Nino3.4 index and the NAO index alone, with the correlation coefficient rising to 0.32 for 68 effective samples, which is above 99% confidence level. Since the SST anomalies in the equatorial eastern Pacific and the NAO are geographically fixed, they together may contribute to the locking phase of the wave train.

8 Impact of the leading wave train on East Asia precipitation and temperature

As shown by Fig. 2a, there are significant positive correlations of rainfall with PC1 over South and East China, with correlations passing the 99% confidence level. To confirm the relation between the wave train and China rainfall anomalies, we compute the regression of circulation onto area-mean monthly rainfalls in South and East China (20–35°N, 105–122°E) based on observed station data (Fig. 11). It reveals that the pattern of the rainfall index-related circulation anomalies at 250-hPa is similar to the EOF1 mode, confirming the tight relationship between the wintertime rainfall anomalies in South and East China and the wave train. At 850-hPa, there exist significant anomalous southerly winds from the Marine Continent to East Asia (Fig. 11b) and exist significant anomalous winds directed from the rainfall region in South and East China through Siberia to Europe, which differs from the low-tropospheric wind anomalies associated with the wave train (figure not shown). This result suggests that the wave train is an important but not the only factor for rainfall anomalies in South and East China. The rainfall could be affected not only by the wave train-induced upward motions but also by low-tropospheric moisture vapor convergence induced by anomalous wind from the tropics (Zhou and Wu 2010; Wang and Feng 2011) and by high-latitude wave activities.

In order to analyze the processes of wave train impact on precipitation, a diagnosis with the linearized omega equation has been performed followed Kosaka and Nakamura (2006):

Fig. 10 Scatter plots of the PC1 index of DJF monthly v at 250-hPa in the domain of 0–45°N, 0–120°E from 1979 to 2013 with DJF monthly Nino3.4 SST index (a), DJF monthly NAO index, and the multi-variant regression: $0.26 \times \text{Nino3.4} + 0.22 \times \text{NAO}$ (c)

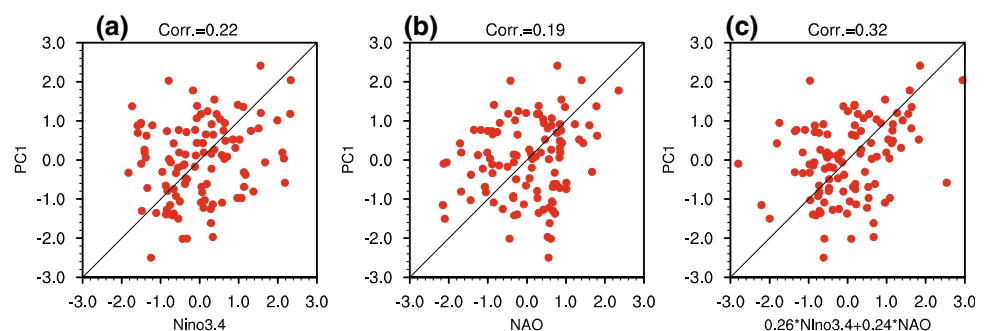


Fig. 11 The regression of precipitation (contours) and winds (vectors; above 95% confidence level) at 250-hPa (a) and 850-hPa (b) on area mean of monthly rainfalls in South and East China (20–35°N, 105–122°E). The gray shades denote regressions above 99% confidence level

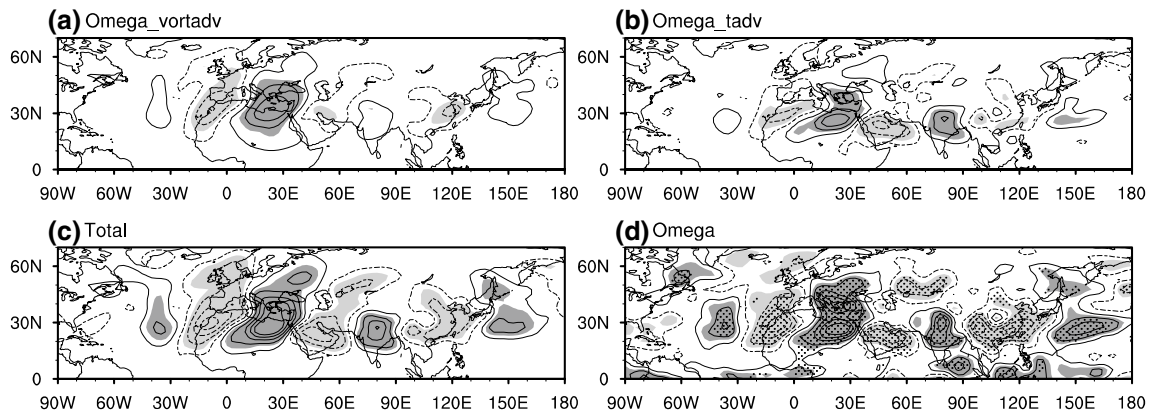
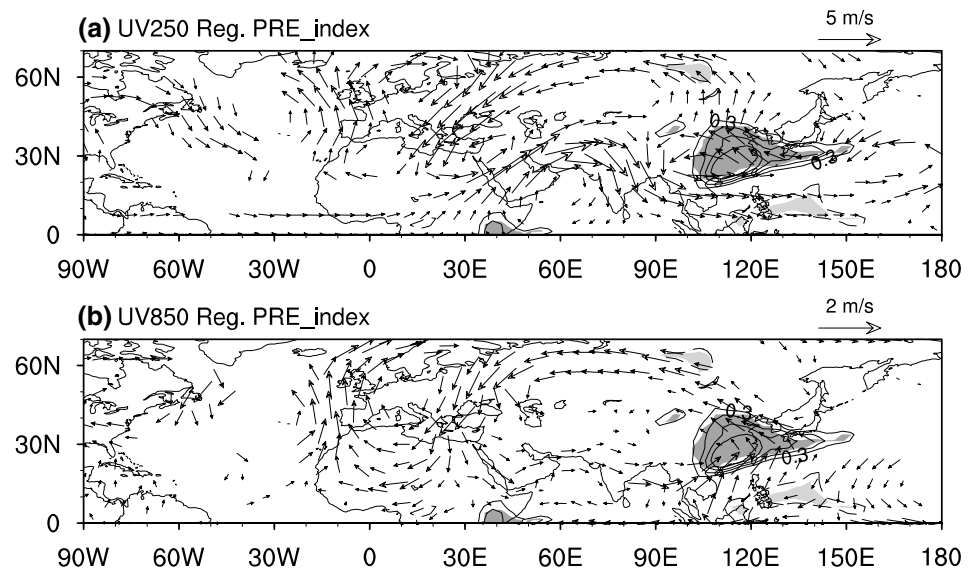


Fig. 12 The DYN term (a), the THE term (b) and their sum (c) at 500 hPa in linearized omega Eq. (8), and the regressions of 500-hPa omega (d) onto normalized PC1. The contours interval in a–d

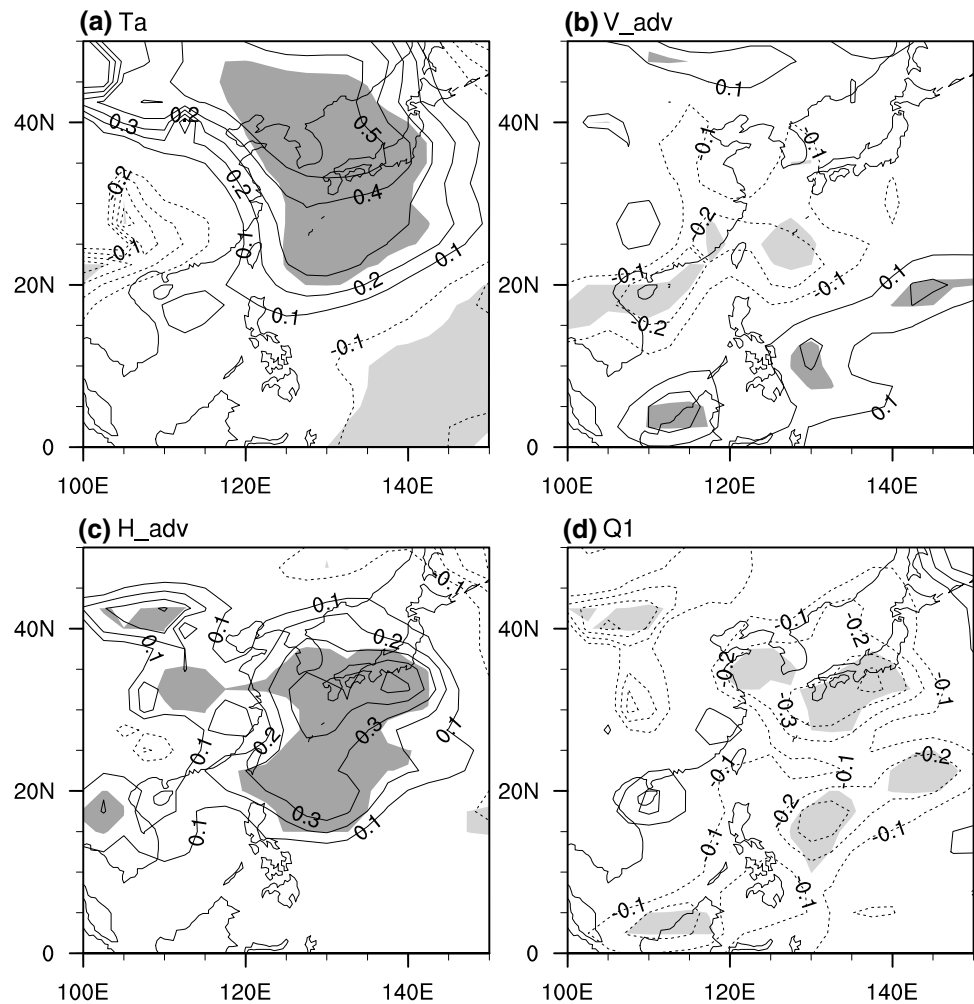
is $0.5 (\pm 0.25, \pm 0.75, \pm 1.25, \dots) \times 10^{-2} \text{ Pas}^{-1}$, with the light gray below $-0.5 \times 10^{-2} \text{ Pas}^{-1}$ and dark gray above $0.5 \times 10^{-2} \text{ Pas}^{-1}$. The dots in d denote regressions above 99% confidence level

$$\omega' = \left(\nabla^2 + \frac{f^2}{\Lambda^2} \frac{\partial^2}{\partial P^2} \right)^{-1} \left\{ \frac{f}{\Lambda} \frac{\partial}{\partial P} [\bar{\mathbf{u}} \cdot \nabla \zeta' + \mathbf{u}' \cdot \nabla (f + \bar{\zeta})] + \frac{R}{\Lambda P} \nabla^2 (\bar{\mathbf{u}} \cdot \nabla T' + \mathbf{u}' \cdot \nabla \bar{T}) \right\}, \quad (8)$$

where overbars and primes indicate climatological mean quantities for DJF mean and the monthly regressed anomalies, respectively. $\Lambda = (R/P) \left(\overline{RT}/C_p P - \overline{dT}/dP \right)$ denotes the static stability. The first term in the right-hand-side of Eq. (8) represents contribution of the vertical difference of vorticity horizontal advection. The second term on the right-hand-side represents the contribution of horizontal temperature advection. For simplicity, we use abbreviations, Omega_vortadv and Omega_tadv, to represent the first and second terms, respectively. Figure 12a–c show the

distribution of the value of Omega_vortadv, Omega_tadv and their sum at 500-hPa. Along the jet, the sum of Omega_vortadv and Omega_tadv (Fig. 12c) agrees well with the 500-hPa vertical velocity anomalies regressed on PC1 (Fig. 12d), indicating that vertical motion anomalies mainly result from the effect of vorticity advection and temperature advection. The small difference between the two patterns of omega in Fig. 12c, d is possibly because the effect of adiabatic heating is not included in Eq. 8. Over South and East China, Omega_vortadv and Omega_tadv are comparable. Note that the wave train-induced vertical motion anomalies are not in accordance with precipitation anomalies every well except for in South and East China, possibly because water vapor is ample in South and East China but insufficient in other regions in winter.

Fig. 13 The regression of monthly low-level (vertical average from 1000-hPa to 850-hPa) air temperature (a), vertical temperature advection (b), horizontal temperature advection (c) and atmospheric apparent heat source (d) with the normalized PC1. The unit in (a) is K, and the units in b–d are K/day. The dark (light) gray shades denote positive (negative) regressions above 99% confidence level



The wave train also has a prominent impact on East Asian temperature anomalies. Figure 13a shows the regressions of low-tropospheric (vertical average from 1000 to 850-hPa with the data below topography setting to missing values) temperature onto PC1. Significant positive temperature anomalies are found in the Northeast Asia including Northeast China, Korean Peninsula, and the southern Japan, indicating a weakened East Asian winter monsoon (Wang and Chen 2010, 2014). Figure 13b–d show the regressions of vertical temperature advection, horizontal temperature advection and atmospheric apparent heat source onto PC1. Following the study of Yanai et al. (1973), we used the atmospheric apparent heat source (Q_1) to represent the total diabatic heating, including radiation, latent heating, and surface heat fluxes. Comparing the distribution of each term, it reveals that the pattern of horizontal temperature advection agrees well with the pattern of temperature anomalies. Thus, the temperature anomalies around the Northeast Asia are mainly due to horizontal temperature advection, in response to the lower-troposphere height anomalies around the Japan Sea (Fig. 3c).

9 Summary

In this study, the structure and dynamics of the wave train along wintertime Asian jet are discussed. The first leading EOF mode of the 250-hPa monthly v in boreal winter displays a wave-like pattern along the Asian jet, and is prominent at mid- and upper-troposphere. Consistent with the wave-like pattern, there are eastward wave fluxes from the North Atlantic to Europe, southeastward wave fluxes from Europe to the Arabian Sea with amplifying amplitude, eastward wave fluxes from the Arabian Sea to South China and northeastward wave fluxes from South China to Japan. Along the jet, the advection of perturbation vorticity by the zonal flow tends to be compensated by the β effect, indicating that the essence of teleconnection pattern is basically a stationary Rossby wave. Analyses suggest that the perturbations of the wave train can extract kinetic energy and available potential energy from climatological mean flow effectively, especially in the region from Europe to the Middle East. Moreover, we found that the efficiency of energy conversions drops quickly when the pattern of wave

train is shifted eastward or westward from its original location. In addition, there exists a positive feedback between transient eddies and the perturbations of the wave train over the North Atlantic and Europe: the stationary circulation associated with the wave train modulates the strength and trajectory of transient eddies, which in turn reinforce the background flow through eddy vorticity transports. The results indicate that the wave train is likely an atmospheric internal mode, which can be developed without external forcing. We also found that El Niño-like SST anomalies in the eastern Pacific and the NAO can exert influences in the wave train, which may help to predict the wave train several months in advance. Both the internal energy conversions and external forcing contribute to the geographic fixing of the phase of the wave train.

The wave train can exert prominent influences in East Asian winter climate. When the wave train is in the phase with a cyclone over South China and an anticyclone over Japan, the rainfall is significant above normal in South and East China, and the temperature is significant above normal over the Northeast Asia, and vice versa. The wave train-induced horizontal temperature advections and vorticity advections together lead to anomalous vertical motions, which in turn lead to rainfall anomalies in wet South and East China. And the wave train-related lower-tropospheric anticyclonic (cyclonic) anomalies over the Northeast Asia lead to warm (cold) temperature advections, resulting in warm (cold) winters in Northeast Asia.

Acknowledgements We thank two anonymous reviewers for their helpful comments. This work was supported by the National Natural Science Foundation of China (41425019, 41661144016, 41275081 and 41205049) and the public science and technology research funds projects of ocean (201505013).

References

- Adler RF et al (2003) The version-2 global precipitation climatology project (GPCP) monthly precipitation analysis (1979–Present). *J Hydrometeorol* 4:1147–1167
- Branstator G (2002) Circumglobal teleconnections, the jet stream waveguide, and the North Atlantic Oscillation. *J Clim* 15:1893–1910
- Chen G, Huang R (2012) Excitation mechanisms of the teleconnection patterns affecting the July precipitation in Northwest China. *J Clim* 25:7834–7851
- Ding Q, Wang B (2005) Circumglobal teleconnection in the Northern Hemisphere Summer*. *J Clim* 18:3483–3505
- Enomoto T, Hoskins BJ, Matsuda Y (2003) The formation mechanism of the Bonin high in August. *Q J Roy Meteor Soc* 129:157–178
- Gill AE (1980) Some simple solutions for heat-induced tropical circulation. *Q J Roy Meteor Soc* 106:447–462
- Hoskins BJ, Ambrizzi T (1993) Rossby wave propagation on a realistic longitudinally varying flow. *J Atmos Sci* 50:1661–1671
- Hoskins BJ, James IN, White GH (1983) The shape, propagation and mean-flow interaction of large-scale weather systems. *J Atmos Sci* 40:1595–1612
- Huang G, Liu Y, Huang R (2011) The interannual variability of summer rainfall in the arid and semiarid regions of Northern China and its association with the northern hemisphere circumglobal teleconnection. *Adv Atmos Sci* 28:257–268
- Kanamitsu M, Ebisuzaki W, Woollen J, Yang SK, Hnilo J, Fiorino M, Potter G (2002) Ncep-doe amip-ii reanalysis (r-2). *B Am Meteorol Soc* 83:1631–1644
- Kosaka Y, Nakamura H (2006) Structure and dynamics of the summertime Pacific–Japan teleconnection pattern. *Q J Roy Meteor Soc* 132:2009–2030
- Kosaka Y, Nakamura H, Watanabe M, Kinoto M (2009) Analysis on the dynamics of a wave-like teleconnection pattern along the summertime Asian jet based on a reanalysis dataset and climate model simulations. *J Meteorol Soc Jpn* 87:561–580
- Lau N-C, Nath MJ (2014) Model simulation and projection of European heat waves in present-day and future climates. *J Clim* 27:3713–3730
- Li Y, Lau N (2012) Impact of ENSO on the atmospheric variability over the North Atlantic in late winter—role of transient eddies. *J Clim* 25:320–342
- Li C, Sun J (2015) Role of the subtropical westerly jet waveguide in a southern China heavy rainstorm in December 2013. *Adv Atmos Sci* 32:601–612
- Li X, Zhou W (2016) Modulation of the interannual variation of the India–Burma Trough on the winter moisture supply over Southwest China. *Clim Dyn* 46:147–158
- Lin H, Derome J, Brunet G (2005) Tropical Pacific link to the two dominant patterns of atmospheric variability. *Geophys Res Lett* 32:L03801. doi:[10.1029/2004GL021495](https://doi.org/10.1029/2004GL021495)
- Liu Y, Wang L, Zhou W, Chen W (2014) Three Eurasian teleconnection patterns: spatial structures, temporal variability, and associated winter climate anomalies. *Clim Dyn* 42:2817–2839
- Lu R, Oh J, Kim B (2002) A teleconnection pattern in upper-level meridional wind over the North African and Eurasian continent in summer. *Tellus A* 54:44–55
- Matsuno T (1966) Quasi-geostrophic motions in the equatorial area*. *J Meteorol Soc Jpn* 44:25–43
- Metz W (1991) Optimal relationship of large-scale flow patterns and the barotropic feedback due to high-frequency eddies. *J Atmos Sci* 48:1141–1159
- North GR, Bell TL, Cahalan RF, Moeng FJ (1982) Sampling errors in the estimation of empirical orthogonal functions. *Mon Weather Rev* 110:699–706. doi:[10.1175/1520-0493\(1982\)110<0699:SEITEO>2.0.CO;2](https://doi.org/10.1175/1520-0493(1982)110<0699:SEITEO>2.0.CO;2)
- Sardeshmukh PD, Hoskins BJ (1988) The Generation of global rotational flow by steady idealized tropical divergence. *J Atmos Sci* 45:1228–1251
- Sato N, Takahashi M (2006) Dynamical processes related to the appearance of quasi-stationary waves on the subtropical jet in the mid-summer Northern Hemisphere. *J Clim* 19:1531–1544
- Song J, Li C, Zhou W (2013) High and low latitude types of the downstream influences of the North Atlantic Oscillation. *Clim Dyn* 42:1097–1111
- Song L, Wang L, Chen W, Zhang Y (2016) Intraseasonal variation of the strength of the East Asian trough and its climatic impacts in boreal winter. *J Clim* 29:2557–2577
- Takaya K, Nakamura H (2001) A formulation of a phase-independent wave-activity flux for stationary and migratory quasigeostrophic eddies on a zonally varying basic flow. *J Atmos Sci* 58:608–627
- Wang L, Chen W (2010) How well do existing indices measure the strength of the East Asian winter monsoon? *Adv Atmos Sci* 27:855–870
- Wang L, Chen W (2014) An intensity index for the East Asian winter monsoon. *J Clim* 27:2361–2374
- Wang L, Feng J (2011) Two major modes of the Wintertime Precipitation over China. *Chin J Atmos Sci* 35:1105–1116

- Watanabe M (2004) Asian jet waveguide and a downstream extension of the North Atlantic oscillation. *J Clim* 17:4674–4691. doi:[10.1175/JCLI-3228.1](https://doi.org/10.1175/JCLI-3228.1)
- Yanai M, Esbensen S, Chu JH (1973) Determination of bulk properties of tropical cloud clusters from large-scale heat and moisture budgets. *J Atmos Sci* 30:611–627
- Yu B, Lin H (2016) Tropical atmospheric forcing of the wintertime North Atlantic oscillation. *J Clim* 29:1755–1772
- Zhou LT, Wu R (2010) Respective impacts of East Asian winter monsoon and ENSO on winter rainfall in China. *J Geophys Res* 115:D02107